# Supplementary Information: Characterising the Ionic Transport and Thermodynamic Properties of Potassium-ion Electrolytes

Shobhan Dhir[1,2], Ben Jagger[1,2], Alen Maguire[1], and Mauro Pasta[1*]

[1]Department of Materials, University of Oxford, OX1 3PH, UK
[2]These authors contributed equally
[*]Corresponding author: mauro.pasta@materials.ox.ac.uk

## Contents

**Supplementary Methods** **2**

1: Densitometry . . . . . 2

2: Hittorf Method . . . . . 3

3: Ionic Conductivity . . . . . 3

4: Concentration Cell . . . . . 3

5: Restricted Diffusion . . . . . 4

6: Error Analysis . . . . . 5

7: Property Parameterisation . . . . . 7

**Supplementary Discussion** **7**

1: Potassium Metal Electrodes . . . . . 8

2: X-ray Photoelectron Spectroscopy . . . . . 8

3: Partial Molar Volumes . . . . . 12

4: Transference Number . . . . . 13

5: Ionic Conductivity . . . . . 15
6: Thermodynamic Factor . . . . . 17
7: Salt Diffusivity . . . . . 20
8: Stefan-Maxwell Diffusion Coefficients . . . . . 22
9: Potassium SEI Instability . . . . . 22

**Supplementary Notes** **23**

1: LiFSI in DME Property Parameterisation . . . . . 23
2: KFSI in DME Property Parameterisation . . . . . 24

**Supplementary References** **25**

# Supplementary Methods

## Supplementary Methods 1: Densitometry

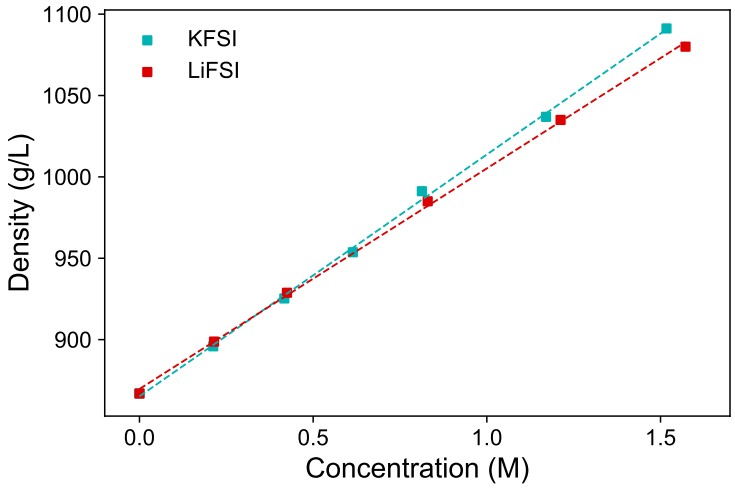


**Supplementary Fig. 1** Density correlations for KFSI and LiFSI in DME at 20°C

## Supplementary Methods 2: Hittorf Method

The Hittorf method is a technique which measures the change in moles of cations, compared to anions, across the cell with the passage of a set amount of charge. The transference number is directly related to the ratio between this change in moles and charge passed. The densitometric Hittorf cell, designed by Hou and Monroe, was used to characterise the transference number.[1] The large cell is isolated into three chambers using stopcocks after polarization and the density differences between these chambers are measured to calculate the concentration differences and hence determine the transference number using Eq. 1.[1] The vertical orientation and direction of polarisation ensures cation flux directly opposes the direction of gravity, preventing the effects of natural convection affecting the measurement due to density gradients.[2]

## Supplementary Methods 3: Ionic Conductivity

The ionic conductivities in Fig. 3b were fitted with the function proposed by Casteel and Amis (Supplementary Eq. 1):[3]

$$\kappa(c) = \kappa_{max} \left( \frac{c}{c_{max}} \right)^{x_1} \exp \left( x_2 (c - c_{max})^2 - \frac{x_1}{c_{max}} (c - c_{max}) \right) \tag{1}$$

Where $\kappa_{max}$ is the maximum ionic conductivity, $c_{max}$ is the concentration at maximum ionic conductivity, and $x_1$ and $x_2$ are fitting constants.

## Supplementary Methods 4: Concentration Cell

A concentration cell places metallic electrodes into two electrolytes with the same constituents but different compositions in chemical contact, enabling measurement of the OCV that arises between them as a result of the difference in chemical potential from the different salt concentrations.[4] The concentration cell contains two chambers separated by

a porous frit which enables electrochemical contact but significantly reduces interdiffusion. One chamber is filled with a 'reference' solution of constant concentration, while the other chamber contains a 'test' solution with a concentration that varies between experiments.

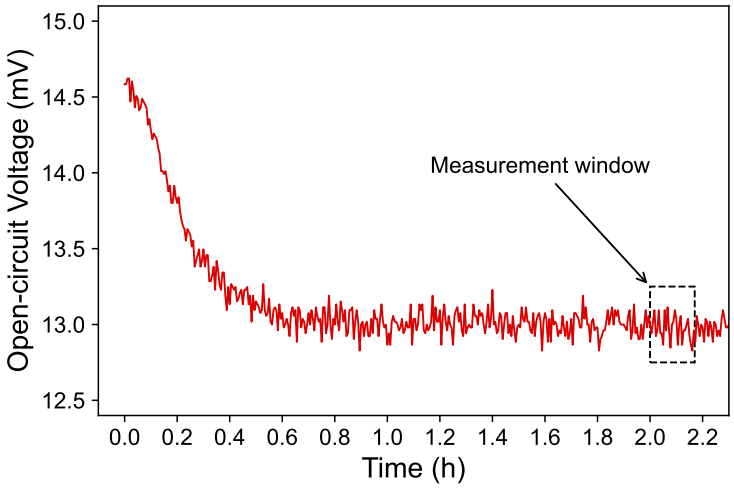


**Supplementary Fig. 2** OCV as a function of time for a representative concentration cell with a 1 m LiFSI in DME 'reference' concentration and a 1.5 m LiFSI in DME 'test' concentration demonstrating the stabilisation of the OCV. The measurement window is visualised by the dashed box

## Supplementary Methods 5: Restricted Diffusion

The restricted diffusion experiment[1,5–8] is the most accurate and reproducible method to measure electrolyte salt diffusion coefficient, $D$, involving a sealed vertically oriented cell where current/potential is applied so stripping occurs at the bottom. The vertical orientation and direction of polarisation again ensures cation flux directly opposes the direction of gravity, preventing the effects of natural convection affecting the measurement due to density gradients.[2] A concentration gradient is induced by galvanostatic polarisation, and the relaxation of the concentration gradient is measured between two points by tracking the OCV. $D$ is determined from this exponential relaxation of OCV using Eq. 4.

In $D$ analysis using the restricted diffusion method, there is some dependence of

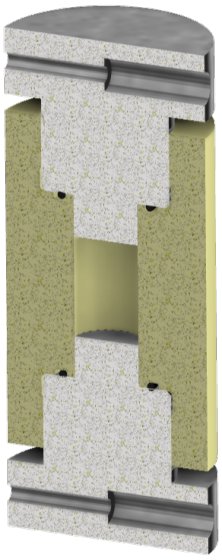

**Supplementary Fig. 3** The designed restricted diffusion cell with polyether ether ketone (PEEK) chamber, stainless steel current collectors and perfluoroelastomer (FFKM) chemically resistant O-rings

the resulting diffusion coefficient on the time window it is fit.[9] Newman and Thomson demonstrated that exponential decay after polarisation occurs for times greater than $0.05l^2/D$ ($\approx 0.5\ \tau_{diff}$), regardless of the initial concentration profile indicating this is the point from which the data should be fit.[10] Therefore, in this analysis the data was fit from this minimum time constant $0.5\ \tau_{diff}$ for as long as it showed exponential relaxation behaviour, or until relaxation had completed. Due to the significantly higher diffusivity of KFSI than LiFSI, this was on average 11 h for KFSI and 33 h for LiFSI. For K-ion electrolytes, due to the reactivity of the K metal, very long analysis time windows occasionally resulted in significant OCV data noise levels or random jumps in potential, similar to what was found for the Na-ion electrolyte $NaPF_6$:EC:DEC.[11] This is attributed to the continued reformation of the SEI on the freshly plated K metal affecting local ion concentration and increasing side reactions, as evidenced by the increasing impedance in Supplementary Fig. 20.

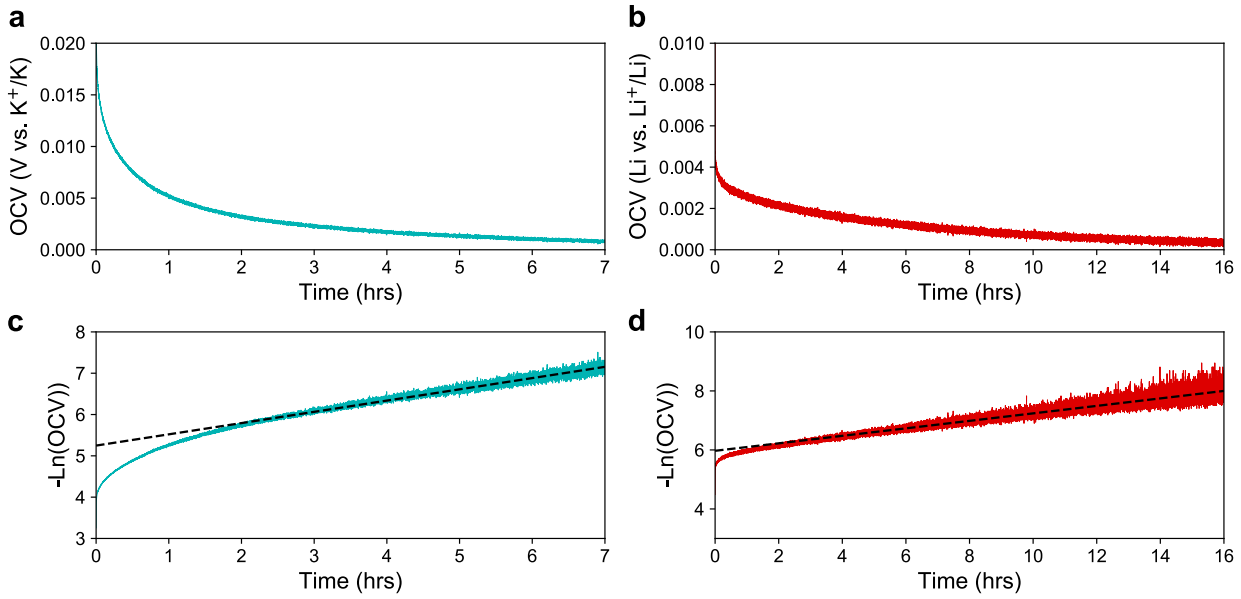


**Supplementary Fig. 4** Representative restricted diffusion open-circuit voltage relaxation data for 1m in DME at 20°C (**a**) KFSI (**b**) LiFSI. Open-circuit voltage data adjusted for $V_{offset}$. Semi-log plot with fitted linear decay region (black dashed line) used to determine salt diffusion coefficient (**c**) KFSI (**d**) LiFSI

.

## Supplementary Methods 6: Error Analysis

The error bars in Fig. 2a, 4a and 5a represent the standard error in the mean, $\sigma_{\overline{x}}$, estimated from the sample standard deviation, $\sigma_x$, and the number of data points, $n$, using Supplementary Eq. 2:

$$\sigma_{\overline{x}} = \frac{\sigma_x}{\sqrt{n}} \tag{2}$$

Due to the high sensitivity of the calculated transference numbers to changes in solution densities, the limited resolution of the density meter results in transference numbers with a non-negligible uncertainty. Each calculated transference number can take any value between $t^0_{+,min}$ and $t^0_{+,max}$, with equal probability, giving each measurement, $i$, an uncertainty variance, $\sigma_i^2$, of $\frac{1}{12}(t^0_{+,max} - t^0_{+,min})^2$. The error in the mean $t^0_+$, $\sigma_{\overline{x}}$, was then estimated by taking into account the sample standard deviation, $\sigma_x$, and the uncertainty variance, $\sigma_i^2$, for each of the

$n$ data points through Supplementary Eq. 3:

$$\sigma_{\overline{x}} = \sqrt{\frac{\sigma_x^2}{n} + \frac{1}{n^2}\sum_{i=1}^{n}\sigma_i^2} \tag{3}$$

Estimated errors in $D$ and $t_+^0$ were then propagated through to $\chi_M$, and the thermodynamic and Stefan-Maxwell diffusivities using the standard propagation rules given in Supplementary Eq. 4:

$$x = \frac{uv}{w}, \quad \sigma_x = x\sqrt{\left(\frac{\sigma_u}{u}\right)^2 + \left(\frac{\sigma_v}{v}\right)^2 + \left(\frac{\sigma_w}{w}\right)^2} \tag{4}$$

## Supplementary Methods 7: Property Parameterisation

All transport and thermodynamic properties were parameterised by fitting functions to the data points. If the functional form was known (Supplementary Eq. 1 for $\kappa$) then non-linear least squares fitting was used. Otherwise, least squares polynomial fits were used, with inverse variance weighting for the case of $t_+^0$.

The parameterised forms of $t_+^0$, $\kappa$, $\chi_M$ and $D$ are given as a function of concentration (either molar, $c$, or molal, $c_m$) for LiFSI and KFSI in DME in Supplementary Notes 1 and 2, respectively. All fits are from data gathered in the concentration range 0.25–2 m.

Approximate conversions between molal and molar concentrations are also provided.

# Supplementary Discussion

## Supplementary Discussion 1: Potassium Metal Electrodes

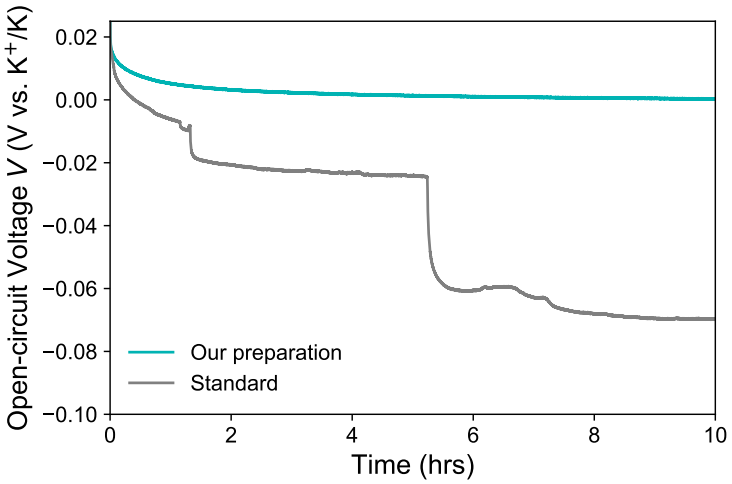


**Supplementary Fig. 5** Diffusion open-circuit potential relaxation profile after 10 h rest and 20 h galvanostatic polarisation in representative K||K symmetric cells in 1 m KFSI:DME in our restricted diffusion cell (Supplementary Fig. 3) using our K preparation compared to standard K preparation (Methods) at 20°C

Characterising the electrolyte $D$ using the leading restricted diffusion method requires exponential OCV relaxation after polarisation of symmetric metal cells (Supplementary Methods 5). Supplementary Fig. 5 shows our K preparation results in exponential OCV relaxation in K symmetric cells, enabling the determination of $D$ from its semi-log plot (Supplementary Fig. 4). The standard preparation cannot be used to determine $D$ due to random OCV jumps, irreproducibility and erratic OCV behaviour, indicating side reactions and K instability, matching similar findings occurring for Na-ion electrolytes.[11]

## Supplementary Discussion 2: X-ray Photoelectron Spectroscopy

The O 1s spectra from the standard preparation in Fig. 2c exhibits a broad peak at 533.6 eV as a result of Na KLL Auger electron emission and its relatively large area is consistent

with the large Na 1s peak evident in Supplementary Fig. 8 that increases with sputtering time, and Na is the main species identified throughout the majority of the examined depth (Supplementary Fig. 6a). The three O 1s peaks at binding energies of 527.0, 529.9 and 530.7 eV are attributed to oxide, hydroxide and carbonate environments, respectively. The oxide peak increases in intensity with the Na 1s peak (Supplementary Fig. 6), suggesting it is $Na_2O$. The binding energy of the hydroxide peak is consistent with NaOH, while the carbonate peak appears at a binding energy between those of the $K_2CO_3$ and $Na_2CO_3$ compounds, suggesting both may be present but cannot be resolved.[12]

The C 1s XPS spectra in Fig. 2c demonstrate a very minor carbonate peak around 289 eV and an adventitious carbon peak at 285 eV. There is an additional broad C 1s peak at 282.7 eV, which is characteristic of a carbide species, although we have been unable to conclusively identify its origin.

The O 1s XPS spectra from K metal prepared with our method in Fig. 2d present only a minor Na KLL Auger peak, consistent with the much lower proportion of Na evident at the surface in Supplementary Fig. 7 and 9. The O 1s carbonate and hydroxide peaks appear at 530.4 and 529.3 eV, respectively, consistent with $K_2CO_3$ and KOH.[12,13] After 5 min of $Ar^+$ sputtering the O 1s oxide peak is at 525.5 eV and a second minor oxide peak at 526.5 eV emerges after 25 min of sputtering. This corresponds with a slight increase in the proportion of Na in the sample, so the two peaks are assigned to $K_2O$ at 525.5 eV and $Na_2O$ at 526.5 eV. The C 1s spectra in Fig. 2d also show a minor carbonate peak at 288.4 eV and the adventitious carbon peak at 285 eV, with no evidence of a carbide peak.

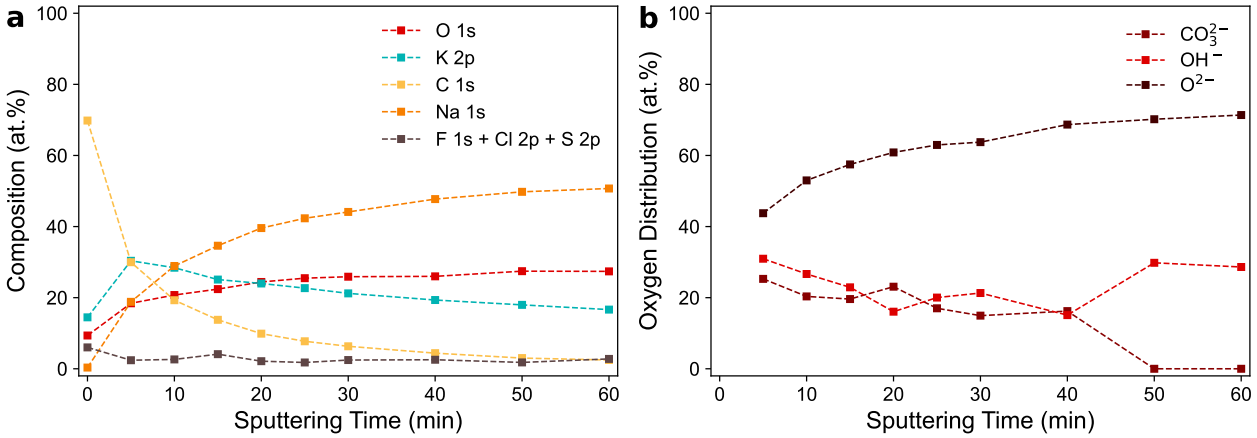


**Supplementary Fig. 6** Quantification of literature preparation K metal electrode composition with sputtering time (**a**) overall composition (**b**) breakdown of oxygen species

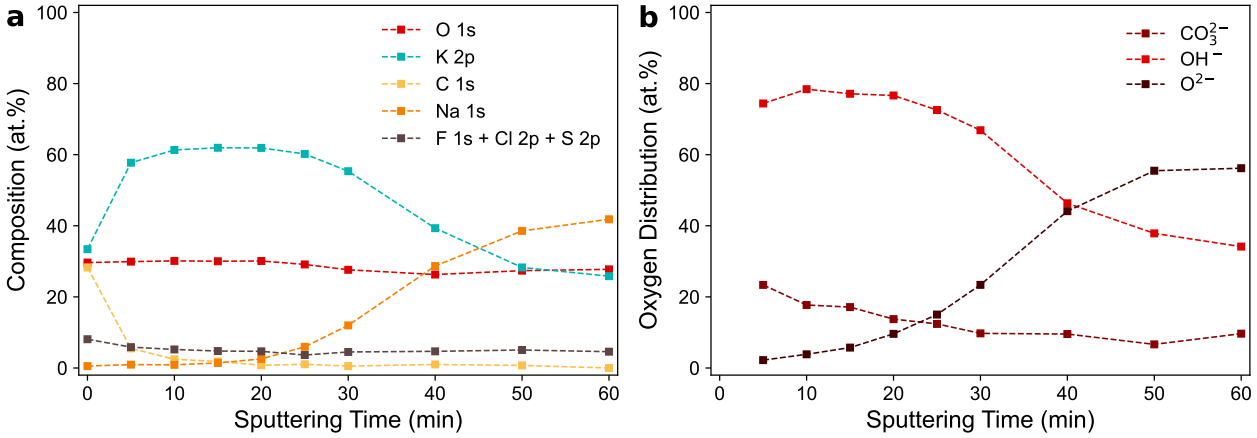


**Supplementary Fig. 7** Quantification of our preparation K metal electrode composition with sputtering time (**a**) overall composition (**b**) breakdown of oxygen species

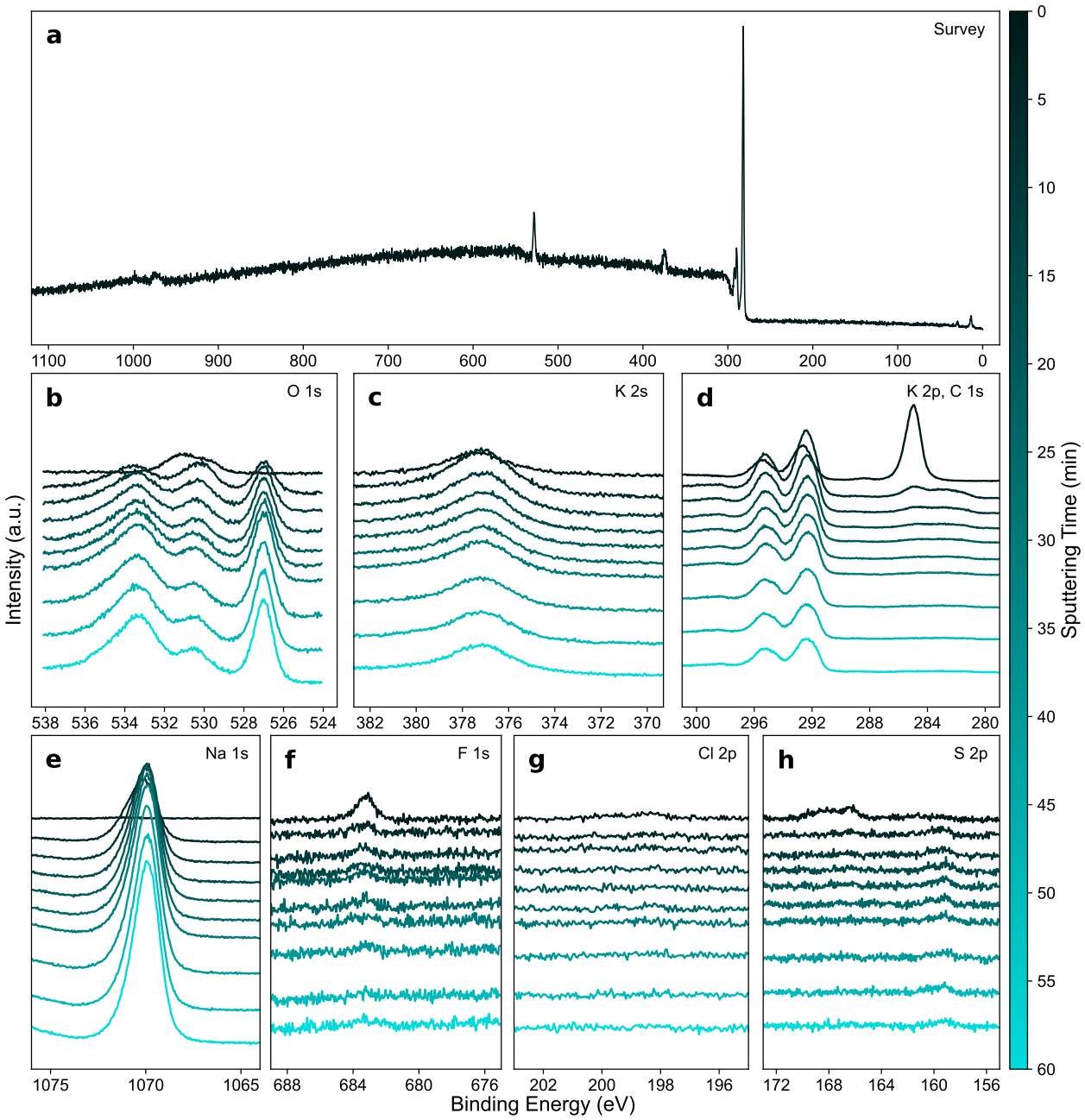


**Supplementary Fig. 8** XPS depth profiles of literature preparation K metal electrode (**a**) survey (**b**) O 1s (**c**) K 2s (**d**) K 2p, C 1s (**e**) Na 1s (**f**) F 1s (**g**) Cl 2p (**h**) S 2p

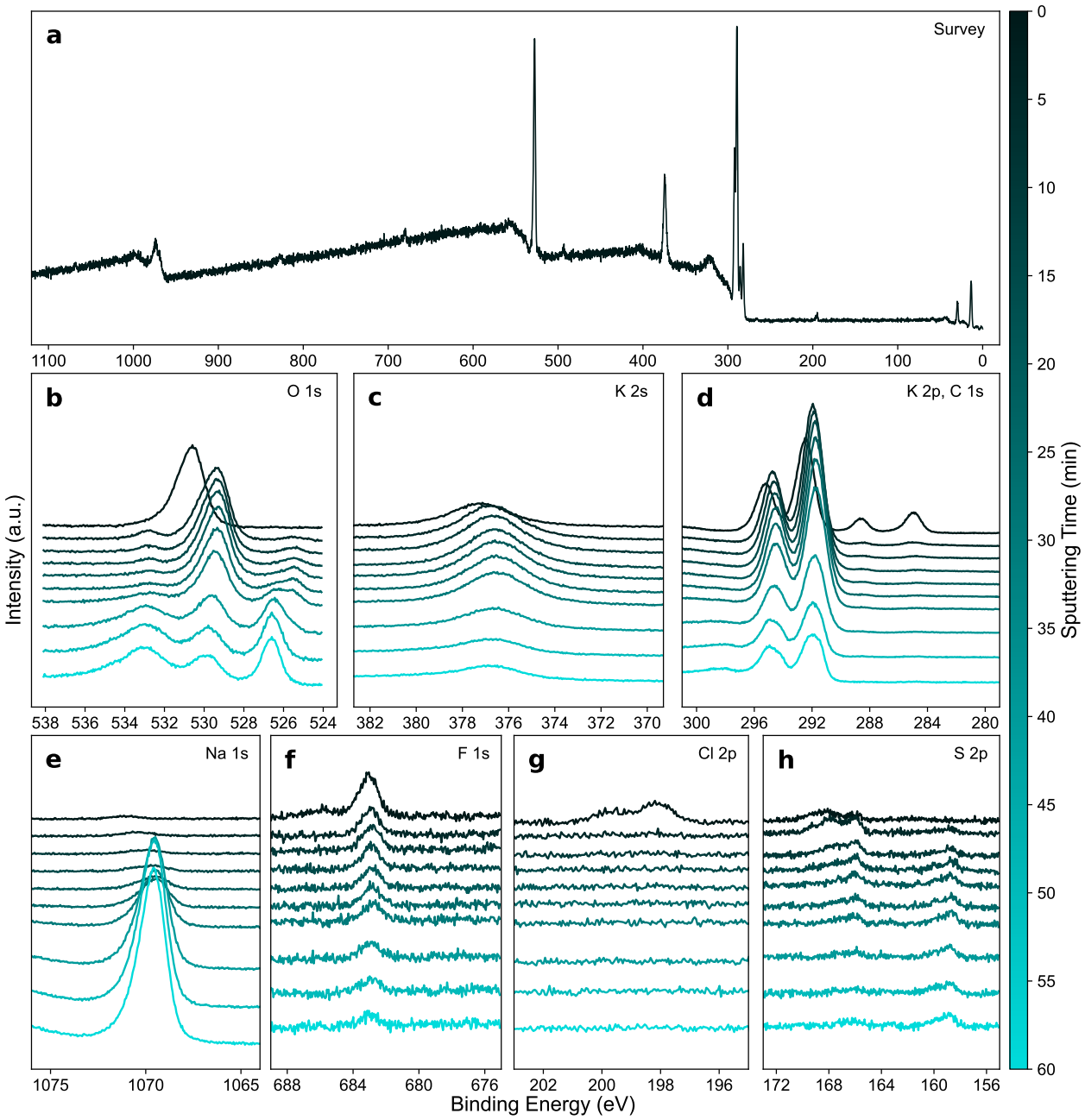


**Supplementary Fig. 9** XPS depth profiles of our preparation K metal electrode (**a**) survey (**b**) O 1s (**c**) K 2s (**d**) K 2p, C 1s (**e**) Na 1s (**f**) F 1s (**g**) Cl 2p (**h**) S 2p

## Supplementary Discussion 3: Partial Molar Volumes

The partial molar volumes of the salt, $\overline{V}_e$, and solvent, $\overline{V}_0$, are calculated from the densitometry results (Supplementary Methods 1) using the following expressions:

$$\overline{V}_e = \frac{M_e - \frac{d\rho}{dc}}{\rho - c\frac{d\rho}{dc}} \tag{5}$$

$$\overline{V}_0 = \frac{M_0}{\rho - c\frac{d\rho}{dc}} \tag{6}$$

where $M_e$ is the molar mass of KFSI/LiFSI, $M_0$ is the molar mass of DME, $\rho$ is the density, $c$ is the molar concentration and $\frac{d\rho}{dc}$ is the slope of the density correlation (Supplementary Fig. 1).

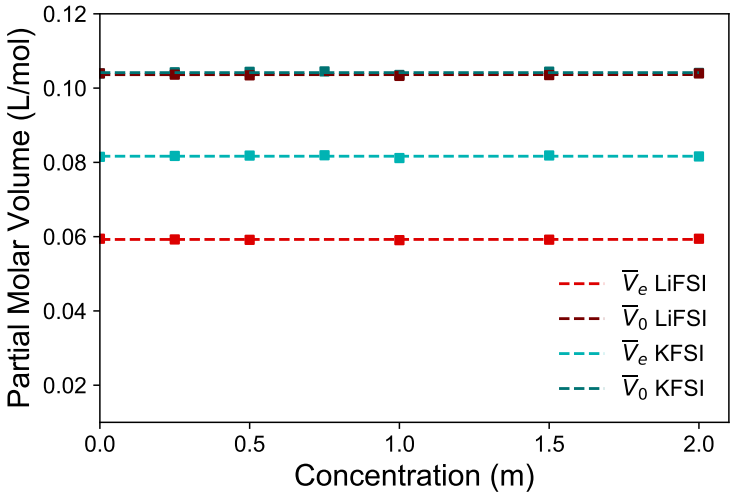


**Supplementary Fig. 10** Partial molar volumes of salt, $\overline{V}_e$, and solvent, $\overline{V}_0$, for LiFSI and KFSI in DME at 20°C

## Supplementary Discussion 4: Transference Number

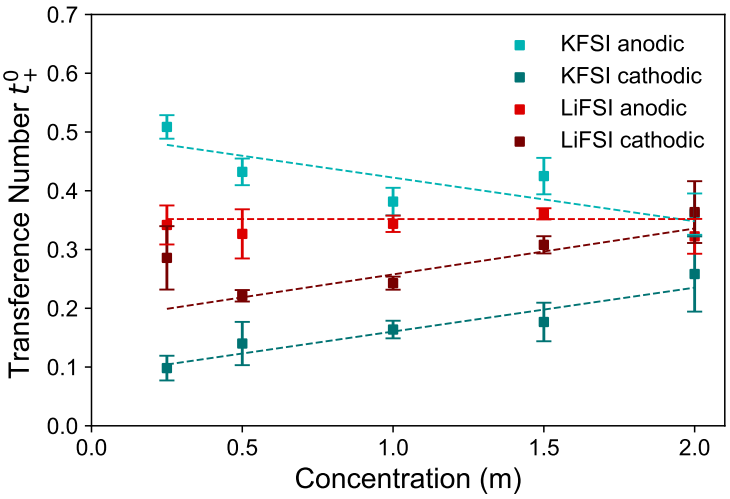


**Supplementary Fig. 11** LiFSI and KFSI cation transference numbers determined from the Hittorf anodic and cathodic chambers in DME at 20°C

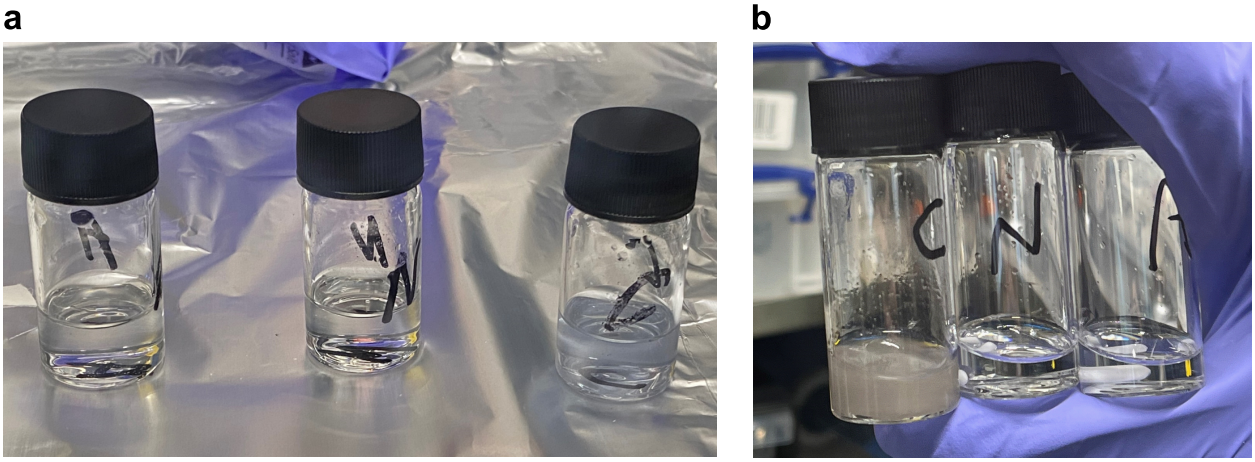


**Supplementary Fig. 12** Cathodic chamber discolouration after Hittorf experiment in DME at 20°C (**a**) KFSI cathodic with neutral and anodic for comparison (**b**) LiFSI cathodic with neutral and anodic for comparison

Due to the volatility of DME, the Hittorf was checked that evaporation did not have any impact over the experiment by running a test cell with no metal electrodes or current applied, filled with electrolyte and measuring the resultant density of the electrolyte before and in

each chamber after. There was no change in density showing DME evaporation is not an issue.

## Supplementary Discussion 5: Ionic Conductivity

The equivalent conductance, $\Lambda$, of both electrolytes was calculated from the ionic conductivity, $\kappa$, and molar concentration, $c$, using Supplementary Eq. 7[14] and is plotted in Supplementary Fig. 13.

$$\Lambda = \frac{\kappa}{z_+ \nu_+ c} \tag{7}$$

Where $z_+$ is the cation charge number and $\nu_+$ is the number of cations into which the salt molecule dissociates.

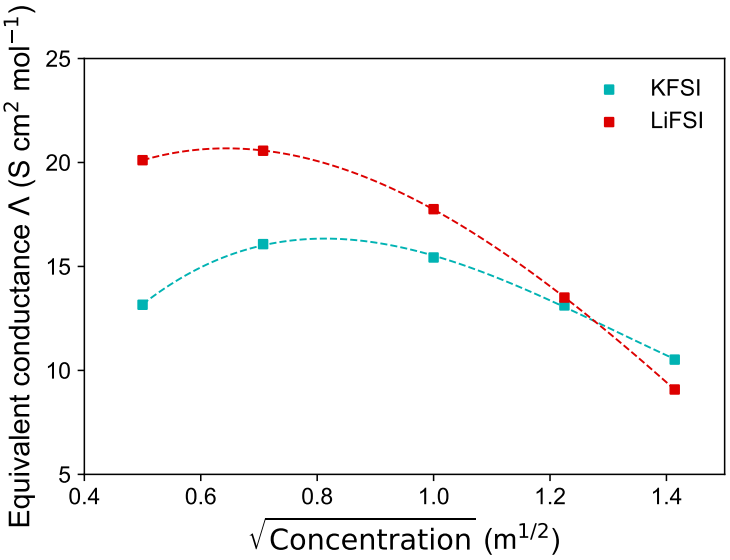


**Supplementary Fig. 13** Equivalent conductance of KFSI and LiFSI in DME at 20°C

The activation energy, $E_a$, was calculated as a function of concentration from the conductivity measurements at three temperatures using Supplementary Eq. 8:[15]

$$\kappa = \kappa_0 e^{-\frac{E_a}{kT}} \tag{8}$$

Where $\kappa_0$ is a constant and $k$ is the Boltzmann constant. The Arrhenius plots used to calculate $E_a$ are shown in Supplementary Fig. 14 and the activation energies are plotted in Supplementary Fig. 15.

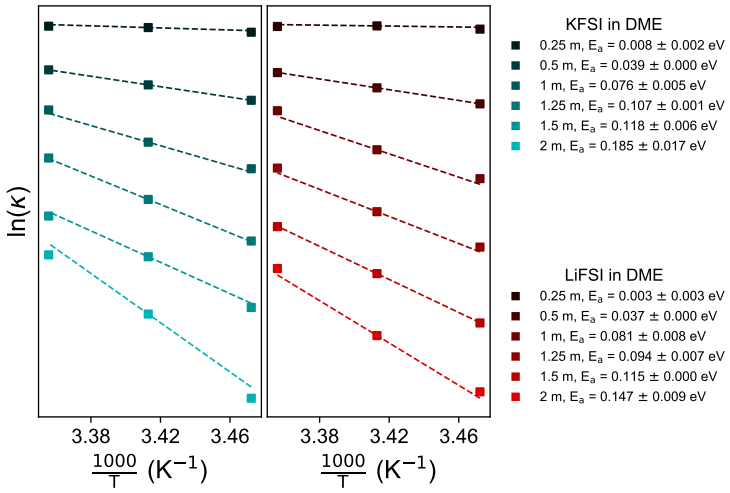


**Supplementary Fig. 14** Arrhenius plots used to calculate the activation energy as a function of concentration. The different concentrations are shifted along the $y$-axis for clarity

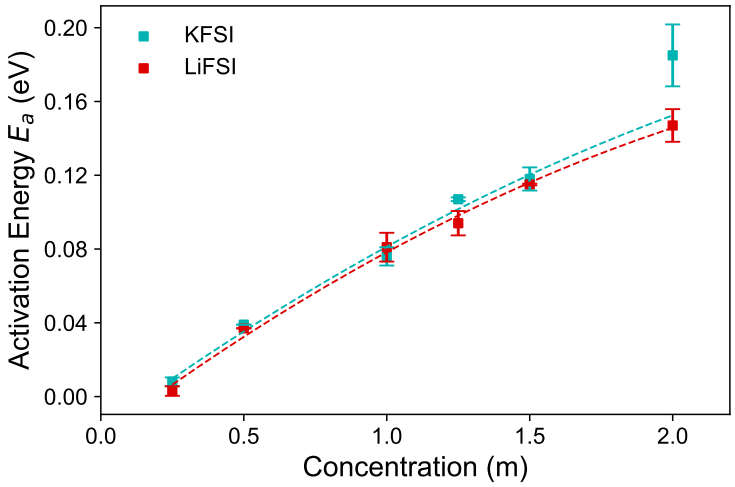


**Supplementary Fig. 15** Activation energies for ionic conduction for KFSI and LiFSI in DME

## Supplementary Discussion 6: Thermodynamic Factor

The thermodynamic factor, $\chi_M$, is related to the change in the OCV measured across the concentration cells, $V$, with the molar concentration of the 'test' electrolyte, $c$, by Supplementary Eq. 9:[4]

$$\chi_M = 1 + \frac{d\ln(f_\pm)}{d\ln(c)} = \frac{F}{2RT(1-t_+^0)}\frac{dV}{d\ln(c)} \tag{9}$$

Where $f_\pm$ is the mean molar activity coefficient, $t_+^0$ is the cation transference number, $F$ is the Faraday constant, $R$ is the gas constant and $T$ is the absolute temperature. The solvent concentration, $c_0$, and the partial molar volume of the solvent, $\overline{V}_0$, can be used to map the thermodynamic factor to the molar basis from the molal basis in which it is defined.[16] It is also convenient to convert from molar concentration to molal concentration, $c_m$, resulting in Supplementary Eq. 10:

$$\chi_M = \frac{1}{c_0\overline{V}_0}\left(1 + \frac{d\ln(\gamma_\pm)}{d\ln(c_m)}\right) = \frac{F\frac{d\ln(c_m)}{d\ln(c)}}{2RT(1-t_+^0)}\frac{dV}{d\ln(c_m)} \tag{10}$$

Where $\gamma_\pm$ is the mean molal activity coefficient. For a strong, binary electrolyte $\gamma_\pm$ is predicted to vary with $c_m$ according to Supplementary Eq. 11:[16]

$$\frac{d\ln(\gamma_\pm)}{d\ln(c_m)} = \frac{z_+z_-\alpha\sqrt{c_m}}{2(1+Ba\sqrt{c_m})^2} + A_2c_m + \frac{3A_3}{2}{c_m}^{\frac{3}{2}} + \cdots \tag{11}$$

Where the first term on the right-hand side comes from Debye-Hückel theory for the long-range electrical interactions between ions and the following terms account for additional concentrated-solution effects.[2] In Supplementary Eq. 11, $z_i$ is the charge number of species $i$, $\alpha$ and $B$ are constants given by Supplementary Eq. 12, $a$ is the average ionic radius, and $A_n$ are fitting constants.

$$\alpha = \frac{F^2 e\sqrt{2\rho_0}}{8\pi(\varepsilon_r\varepsilon_0 RT)^{3/2}}, \quad B = \frac{F\sqrt{2\rho_0}}{\sqrt{\varepsilon_r\varepsilon_0 RT}} \tag{12}$$

In Supplementary Eq. 12 $e$ is electronic charge, $\rho_0$ is solvent density, $\varepsilon_r$ is relative permittivity of the solvent, and $\varepsilon_0$ is vacuum permittivity. Taking the values for DME ($\rho_0$ = 866.9 g $L^{-1}$, $\varepsilon_r$ = 7.2) gives $\alpha$ = 40.38 $kg^{\frac{1}{2}}$ $mol^{-\frac{1}{2}}$ and $B$ = 10.20 $kg^{\frac{1}{2}}$ $mol^{-\frac{1}{2}}$ $nm^{-1}$ at 20°C.

Combining Supplementary Eq. 10 and 11, and dropping terms beyond $A_2{c_m}^2$ gives Supplementary Eq. 13:

$$\frac{dV}{d\ln(c_m)} = \frac{2RT(1-t_+^0)}{F\frac{d\ln(c_m)}{d\ln(c)}}\frac{1}{c_0\overline{V}_0}\left(1 + \frac{z_+z_-\alpha\sqrt{c_m}}{2(1+Ba\sqrt{c_m})^2} + A_2c_m\right) \tag{13}$$

In both electrolyte systems investigated $\frac{d\ln(c_m)}{d\ln(c)}$ was found to be constant and $\frac{1}{c_0\overline{V}_0}$ was well described by a function of the form $\frac{1}{c_0\overline{V}_0} = 1 + B_1c_m$, where $B_1$ is a constant. Supplementary Eq. 13 was integrated with respect to $\ln(c_m)$, with the boundary condition that $V$ = 0 V at $c_m$ = 1 m, to find an expression for $V$ as a function of $c_m$ that was then fit to the OCV data.

This function is fit to the LiFSI data in Supplementary Fig. 16, taking $t_+^0$ to be constant (Fig. 3a) and assuming $a$ = 0.76 Å, the ionic radius of $Li^+$.[17] However, this resulted in a poor fit to the data.

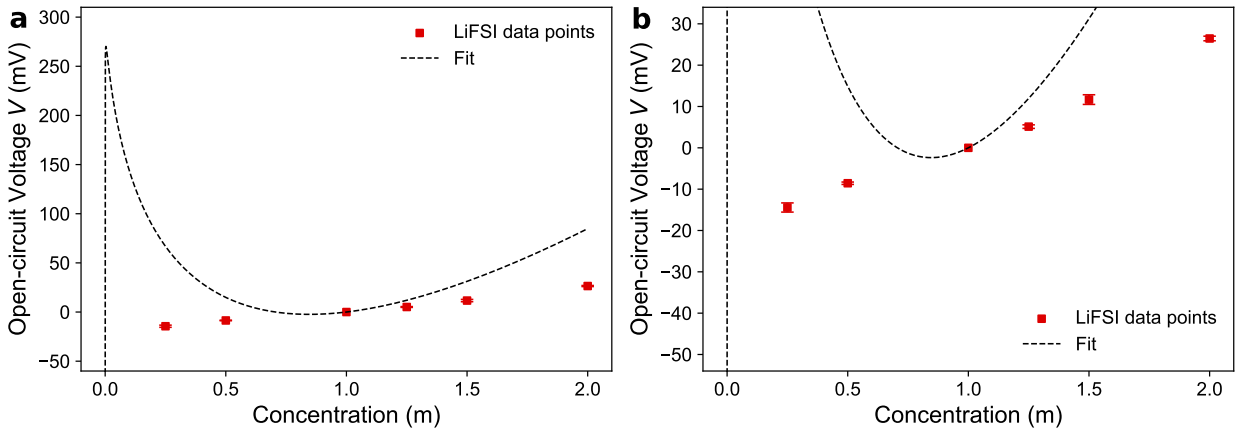


**Supplementary Fig. 16** The fit to the LiFSI concentration cell OCV data determined by Supplementary Eq. 13 (**a**) full scale (**b**) reduced scale

Debye-Hückel theory assumes electrolytes are strong and fully dissociate,[2,14] which we have demonstrated not to be the case for the electrolytes studied here. This can be taken into account by introducing a second fitting constant, $\xi$,[14] to Supplementary Eq. 13, resulting in Supplementary Eq. 14.

$$\frac{dV}{d\ln(c_m)} = \frac{2RT(1-t_+^0)}{F\frac{d\ln(c_m)}{d\ln(c)}}\frac{1}{c_0\overline{V}_0}\left(1+\frac{z_+z_-\alpha\sqrt{\xi c_m}}{2(1+Ba\sqrt{\xi c_m})^2}+A_2c_m\right) \tag{14}$$

$\xi$ can be thought of as a correction factor to the ionic strength, and its introduction leads to a much better fit to the data, as evident in Supplementary Fig. 17a.

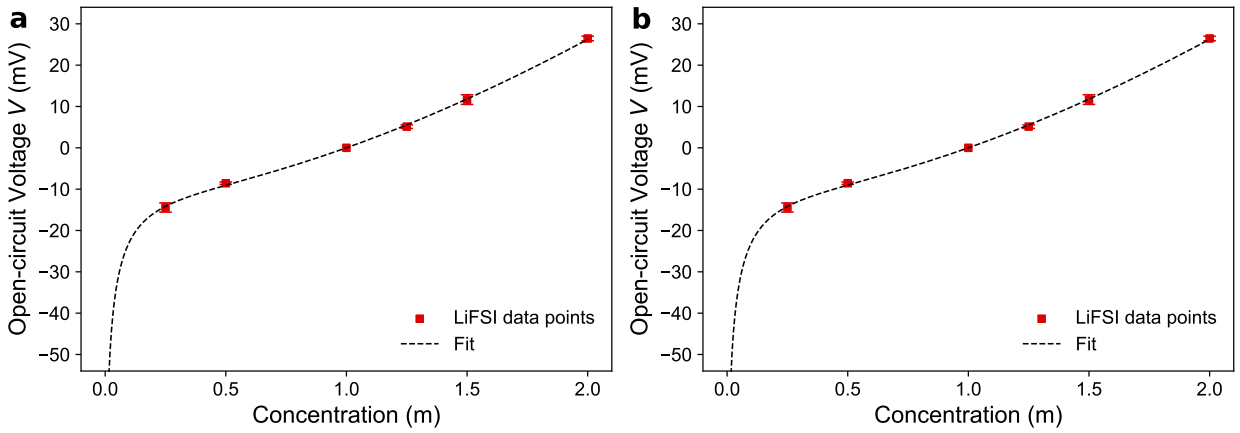


**Supplementary Fig. 17** The fit to the LiFSI concentration cell OCV data determined by (**a**) Supplementary Eq. 14 (**b**) Supplementary Eq. 15

Additionally, the value of $\xi$ determined by the fit is such that $1 + Ba\sqrt{\xi c_m} \approx 1$, allowing Supplementary Eq. 14 to be simplified to Supplementary Eq. 15:

$$\frac{dV}{d\ln(c_m)} = \frac{2RT}{F\frac{d\ln(c_m)}{d\ln(c)}}(1 - t_+^0)\frac{1}{c_0\overline{V}_0}\left(1 + A_1 {c_m}^{\frac{1}{2}} + A_2 c_m\right) \tag{15}$$

Where $A_1$ ($\approx \frac{z_+ z_- \alpha\sqrt{\xi}}{2}$) is a fitting constant. Supplementary Eq. 15 results in just as good a fit to the data in Supplementary Fig. 17b, and allows the concentration dependence of $t^0_{K^+}$ to be taken into account. Once $A_1$ and $A_2$ are fit to the OCV data, $\chi_M$ can be calculated from Supplementary Eq. 16:

$$\chi_M = \frac{1}{c_0\overline{V}_0}(1 + A_1 {c_m}^{\frac{1}{2}} + A_2 c_m) \tag{16}$$

## Supplementary Discussion 7: Salt Diffusivity

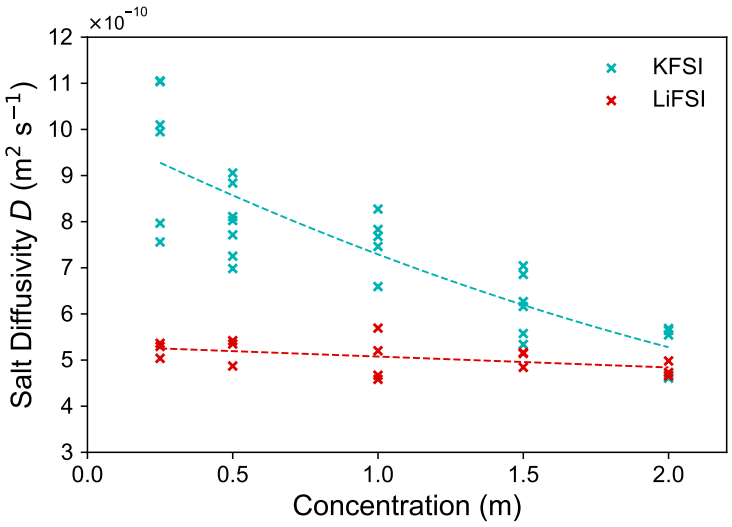


**Supplementary Fig. 18** All salt diffusion coefficient results for KFSI and LiFSI in DME at 20°C

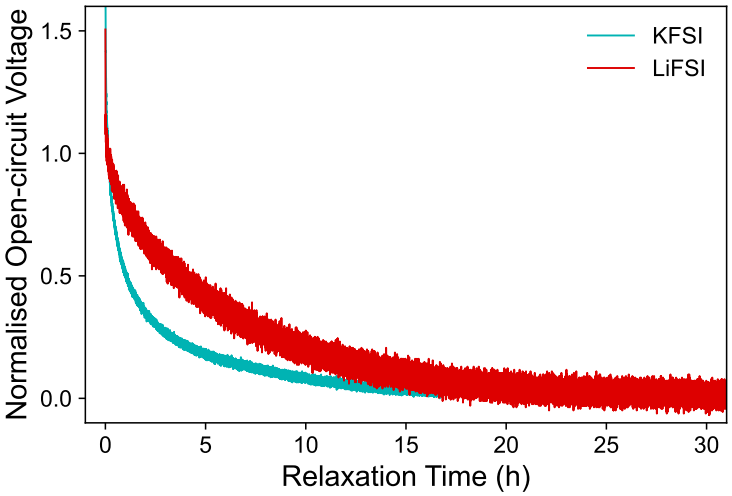


**Supplementary Fig. 19** Relaxation profiles of 0.25 m LiFSI and KFSI in DME, normalised to the potential after 100 s to exclude double layer effects, demonstrating significantly faster relaxation in KFSI

The thermodynamic diffusivity, $\mathscr{D}$, is calculated from $D$, $\chi_M$, total molarity, $c_T$, and partial molar volume of solvent, $\overline{V}_0$, according to Supplementary Eq. 17:[4]

$$\mathscr{D} = \frac{D}{c_T \overline{V}_0 \chi_M} \tag{17}$$

## Supplementary Discussion 8: Stefan-Maxwell Diffusion Coefficients

The Stefan-Maxwell diffusion coefficients provide a more detailed understanding of the diffusional behaviour of each individual electrolyte species and their interactions with other species in solution. The Stefan-Maxwell formalism expresses transport laws through the thermodynamic forces which drive diffusion.[1,14] The coefficients are calculated from the characterised transport properties using the following expressions:[2]

$$\mathscr{D}_{0-} = \frac{z_+}{z_+ - z_-} \frac{\mathscr{D}}{t_+^0} \tag{18}$$

$$\mathscr{D}_{0+} = \frac{-z_-}{z_+ - z_-} \frac{\mathscr{D}}{1 - t_+^0} \tag{19}$$

$$\frac{1}{\mathscr{D}_{+-}} = -\frac{z_+ z_- c_T F^2}{RT\kappa} - \frac{z_+ - z_-}{z_+ \nu_+} \frac{c_0 t_+^0 (1 - t_+^0)}{c\mathscr{D}} \tag{20}$$

Where $\mathscr{D}_{0-}$ and $\mathscr{D}_{0+}$ are the Stefan-Maxwell diffusion coefficients between the solvent and the anion and cation, respectively. $\mathscr{D}_{+-}$ is the Stefan-Maxwell diffusion coefficient between the cation and anion. $c_T$ is the total particle molarity, $c_T = c_0 + c_- + c_+$, where $c_0$ is the solvent molarity ($c_0 = \frac{1-\overline{V}_e}{\overline{V}_0}$), and $c_-$ and $c_+$ are the cation and anion molarity, respectively. $z_i$ and $\nu_i$ are the charge number and the number of ions of species $i$ into which the salt molecule dissociates, respectively.

## Supplementary Discussion 9: Potassium SEI Instability

Supplementary Fig. 20 demonstrates the instability of the solid electrolyte interphase (SEI) that forms on K metal in KFSI:DME electrolytes. The impedance continuously increases over time, indicative of a growing SEI.[18] This suggests electrolyte reduction reactions continue to occur at the K metal-electrolyte interfaces. We found that the SEI was least stable at lower concentration, resulting in a higher impedance.

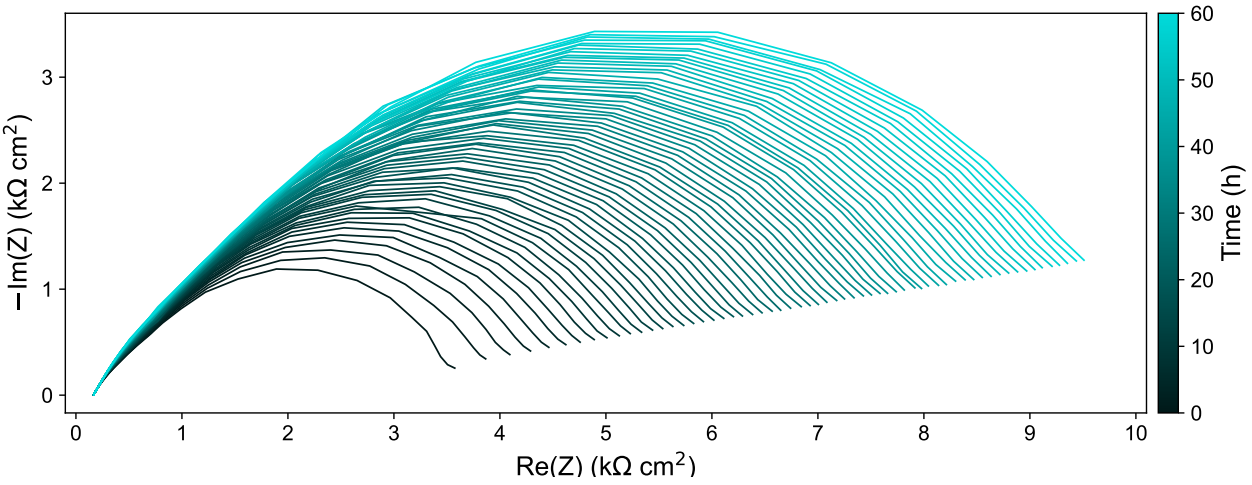


**Supplementary Fig. 20** Impedance plot of K metal symmetric cell with 0.5 m KFSI in DME electrolyte over time during concentration gradient relaxation

# Supplementary Notes

## Supplementary Note 1: LiFSI in DME Property Parameterisation

Cation transference number, $t_+^0$:

$$t_+^0 = 0.352 \tag{21}$$

Ionic conductivity, $\kappa$ (mS cm$^{-1}$):

$$\kappa = 16.286 \left(\frac{c}{1.158}\right)^{1.085} \exp\left(-0.426(c-1.158)^2 - \frac{1.085}{1.158}(c-1.158)\right) \tag{22}$$

Thermodynamic factor, $\chi_M$:

$$\chi_M = (1 + 0.052c_m)(1 - 2.663{c_m}^{\frac{1}{2}} + 2.287c_m) \tag{23}$$

Salt diffusivity, $D$ ($\mathrm{m^2\ s^{-1}}$):

$$D = 5.312 \times 10^{-10} - (2.358 \times 10^{-11})c_m \tag{24}$$

Concentration conversion:

$$c = 0.873c_m - 0.043{c_m}^2 \tag{25}$$

## Supplementary Note 2: KFSI in DME Property Parameterisation

Cation transference number, $t_+^0$:

$$t_+^0 = 0.497 - 0.074c_m \tag{26}$$

Ionic conductivity, $\kappa$ ($\mathrm{mS\ cm^{-1}}$):

$$\kappa = 15.970 \left(\frac{c}{1.493}\right)^{1.620} \exp\left(0.023(c - 1.493)^2 - \frac{1.620}{1.493}(c - 1.493)\right) \tag{27}$$

Thermodynamic factor, $\chi_M$:

$$\chi_M = (1 + 0.071c_m)(1 - 1.833{c_m}^{\frac{1}{2}} + 1.608c_m) \tag{28}$$

Salt diffusivity, $D$ ($\mathrm{m^2\ s^{-1}}$):

$$D = 1.003 \times 10^{-9} - (3.104 \times 10^{-10})c_m + (3.633 \times 10^{-11}){c_m}^2 \tag{29}$$

Concentration conversion:

$$c = 0.859c_m - 0.051{c_m}^2 \tag{30}$$

# Supplementary References


1. Hou, T. & Monroe, C. W. Composition-dependent Thermodynamic and Mass-transport Characterization of Lithium Hexafluorophosphate in Propylene Carbonate. *Electrochim. Acta* **332,** 135085 (2020).
2. Newman, J. & Thomas-Alyea, K. E. *Electrochemical Systems, 3rd Edition* (Wiley, 2004).
3. Casteel, J. F. & Amis, E. S. Specific Conductance of Concentrated Solutions of Magnesium Salts in Water-Ethanol System. *J. Chem. Eng. Data* **17,** 55–59 (1972).
4. Wang, A. A. *et al.* Review of Parameterisation and a Novel Database (LiionDB) for Continuum Li-ion Battery Models. *Prog. Energy* **4,** 032004 (2022).
5. Harned, H. S. & French, D. M. A Conductance Method for the Determination of the Diffusion Coefficients of Electrolytes. *Ann. NY Acad. Sci.* **46,** 267–284 (1945).
6. Newman, J. & Chapman, T. W. Restricted Diffusion in Binary Solutions. *AIChE J* **19,** 343–348 (1973).
7. Ma, Y. *et al.* The Measurement of a Complete Set of Transport Properties for a Concentrated Solid Polymer Electrolyte Solution. *J. Electrochem. Soc.* **142,** 1859–1868 (1995).
8. Ehrl, A., Landesfeind, J., Wall, W. A. & Gasteiger, H. A. Determination of Transport Parameters in Liquid Binary Lithium Ion Battery Electrolytes. *J. Electrochem. Soc.* **164,** A826–A836 (2017).
9. Bergstrom, H. K., Fong, K. D. & McCloskey, B. D. Interfacial Effects on Transport Coefficient Measurements in Li-ion Battery Electrolytes. *J. Electrochem. Soc.* **168,** 060543 (2021).
10. Thompson, S. D. & Newman, J. Differential Diffusion Coefficients of Sodium Polysulfide Melts. *J. Electrochem. Soc.* **136,** 3362–3369 (1989).
11. Landesfeind, J. *et al.* Comparison of Ionic Transport Properties of Non-Aqueous Lithium and Sodium Hexafluorophosphate Electrolytes. *J. Electrochem. Soc.* **168,** 040538 (2021).
12. Caracciolo, L., Madec, L. & Martinez, H. XPS Analysis of K-based Reference Compounds to Allow Reliable Studies of Solid Electrolyte Interphase in K-ion Batteries. *ACS Appl. Energy Mater.* **4,** 11693–11699 (2021).

13. Allgayer, F., Maibach, J. & Jeschull, F. Comparing the Solid Electrolyte Interphases on Graphite Electrodes in K and Li Half Cells. *ACS Appl. Energy Mater.* **5,** 1136–1148 (2022).

14. Wang, A. A., Hou, T., Karanjavala, M. & Monroe, C. W. Shifting-reference Concentration Cells to Refine Composition-dependent Transport Characterization of Binary Lithium-ion Electrolytes. *Electrochim. Acta* **358,** 136688 (2020).

15. Yim, C.-H. & Abu-Lebdeh, Y. A. Connection between Phase Diagram, Structure and Ion Transport in Liquid, Aqueous Electrolyte Solutions of Lithium Chloride. *J. Electrochem. Soc.* **165,** A547–A556 (2018).

16. Stewart, S. & Newman, J. Measuring the Salt Activity Coefficient in Lithium-battery Electrolytes. *J. Electrochem. Soc.* **155,** A458 (2008).

17. Dhir, S., Wheeler, S., Capone, I. & Pasta, M. Outlook on K-Ion Batteries. *Chem* **6,** 2442–2460 (2020).

18. Nojabaee, M., Kuster, K., Starke, U., Popovic, J. & Maier, J. Solid Electrolyte Interphase Evolution on Lithium Metal in Contact with Glyme-Based Electrolytes. *Small* **16,** e2000756 (2020).